On the origin of frequency sparsity in direct numerical simulations of turbulent pipe flow

F. Gómez,[1,a)] H. M. Blackburn,[1] M. Rudman,[1] B. J. McKeon,[2] M. Luhar,[2] R. Moarref,[2] and A. S. Sharma[3]

[1]*Department of Mechanical and Aerospace Engineering, Monash University, Victoria 3800, Australia*
[2]*Graduate Aerospace Laboratories, California Institute of Technology, Pasadena, California 91125, USA*
[3]*Faculty of Engineering and the Environment, University of Southampton, Southampton SO17 1BJ, United Kingdom*

The possibility of creating reduced-order models for canonical wall-bounded turbulent flows based on exploiting energy sparsity in frequency domain, as proposed by Bourguignon *et al.* [Phys. Fluids **26**, 015109 (2014)], is examined. The present letter explains the origins of energetically sparse dominant frequencies and provides fundamental information for the design of such reduced-order models. The resolvent decomposition of a pipe flow is employed to consider the influence of finite domain length on the flow dynamics, which acts as a restriction on the possible wavespeeds in the flow. A forcing-to-fluctuation gain analysis in the frequency domain reveals that large sparse peaks in amplification occur when one of the possible wavespeeds matches the local wavespeed via the critical layer mechanism. A link between amplification and energy is provided through the similar characteristics exhibited by the most energetically relevant flow structures, arising from a dynamic mode decomposition of direct numerical simulation data, and the resolvent modes associated with the most amplified sparse frequencies. These results support the feasibility of reduced-order models based on the selection of the most amplified modes emerging from the resolvent model, leading to a novel computationally efficient method of representing turbulent flows. © *2014 AIP Publishing LLC*. [http://dx.doi.org/10.1063/1.4900768]

A compact representation of turbulent pipe flow based on compressive sampling has been recently carried out by Bourguignon *et al.*[1] This representation relies on sparsity properties of the flow in frequency domain, in the sense that only a small number of frequencies, widely spaced, are energetically dominant. Correspondingly, the success of the applicability of compressive sampling techniques to turbulent flows indicated that these flows admit a sparse representation which is inherent to the discrete treatment of wall-bounded turbulence. As a consequence, sparsity patterns in frequency of the energy spectrum of turbulent pipe flow have been identified through compressive sampling of Fourier transformed velocity fields obtained via direct numerical simulations (DNS).[1] These findings enable the possibility of novel efficient reduced-order models based on selecting energetically dominant modes from this set of sparse frequencies, which could provide progress in the quest for further understanding or controlling wall-bounded turbulent flows.

The present work focuses on an investigation of the origin and understanding of these energy sparsity patterns, based on a turbulent pipe flow from a DNS dataset computed for $R^+ = 314$. An extension of the input-output amplification analysis of the resolvent framework[2] able to deal with finite period length domains in an implicit way is employed for this purpose. Previous success of the resolvent model developed by McKeon, Sharma, and co-workers[2–6] covers the identification of

---

a)francisco.gomez-carrasco@monash.edu

coherent structures and the reproduction and scaling of wall-bounded turbulence features by means of the interaction of such coherent structures. Furthermore, this model permits the decomposition of the velocity fields as a sum of weighted resolvent modes associated with a particular set of wavenumbers and frequencies, which favor sparse decompositions of the velocity fields, as shown by Bourguignon *et al.*[1] Additionally, this energy-based decomposition is directly obtained from the Navier–Stokes equations, as opposed to other data-dependent models, such as proper orthogonal decomposition (POD)[7] or dynamic mode decomposition[8,9] (DMD). As an aid to understanding, standard time domain frequency and DMD analyses are carried out on the turbulent DNS data and the results obtained are compared to the resolvent model.

An extension to the resolvent model is elaborated below. The pipe flow is governed by the incompressible Navier–Stokes equations in non-dimensional form,

$$\nabla \cdot \hat{\mathbf{u}} = 0, \tag{1}$$

$$\frac{\partial \hat{\mathbf{u}}}{\partial t} + \hat{\mathbf{u}} \cdot \nabla \hat{\mathbf{u}} = -\nabla p + Re^{-1}\nabla^2 \hat{\mathbf{u}}, \tag{2}$$

where Re is the Reynolds number based on the bulk velocity and pipe diameter D, $\hat{\mathbf{u}} = (u, v, w)$ is the velocity vector expressed in cylindrical coordinates (x, r, θ) and p is the modified pressure. The mean flow $\mathbf{u_0} = (u_0, 0, 0)$ is obtained from the DNS and subtracted from the total velocity to leave the fluctuating velocity $\mathbf{u} = \hat{\mathbf{u}} - \mathbf{u_0}$, which may be decomposed as a sum of Fourier modes,

$$\mathbf{u}(x, r, \theta, t) = \sum_n \int_\omega \mathbf{u}_{n,\omega}(x, r) e^{i(n\theta - \omega t)} \mathrm{d}\omega, \tag{3}$$

where n and ω are the non-dimensional azimuthal wavenumber and the temporal frequency respectively. Similarly, the nonlinear convective terms are Fourier-transformed as $\mathbf{f}_{n,\omega} = (\mathbf{u} \cdot \nabla \mathbf{u})_{n,\omega}$. Notice that, in contrast with the classical *one-dimensional* resolvent formulation,[2] homogeneity of the pipe flow in the axial direction has not been exploited and the axial coordinate x has not been Fourier-transformed into an axial wavenumber k, thus this *two-dimensional* resolvent formulation permits the general analysis of flows non-homogeneous in the axial direction as well as taking into account the finite length of the computational periodic domain employed in the DNS. While initially it appears redundant to introduce a two-dimensional formulation for a smooth straight pipe flow, we will demonstrate that this treatment allows new insight to be gained from a numerical point of view in a convenient way, as this model possesses the same computational domain as that employed in the DNS. Nevertheless, we are aware that a careful use of the classical resolvent would yield the same outcome by imposing discrete axial wavenumbers, as will be demonstrated.

A manipulation of (2) with the above Fourier decompositions of the fluctuation velocity yields the linear relation

$$\mathbf{u}_{n,\omega}(x, r) = \mathcal{H}_{n,\omega} \mathbf{f}_{n,\omega}(x, r), \tag{4}$$

for each (n, ω) combination. The operator $\mathcal{H}_{n,\omega}$ is known as the resolvent and depends solely on the mean flow and its spatial derivatives; it acts as a transfer function between the fluctuating velocity and the nonlinear terms, in which the nonlinear terms are considered as the forcing that drives the fluctuations. A singular value decomposition (SVD) of the resolvent operator

$$\mathcal{H}_{n,\omega} = \sum_m \boldsymbol{\psi}_{n,\omega,m} \sigma_{n,\omega,m} \boldsymbol{\phi}_{n,\omega,m}^* \tag{5}$$

provides an optimal set of orthonormal singular response modes $\boldsymbol{\psi}_{n,\omega,m}$ and singular forcing modes $\boldsymbol{\phi}_{n,\omega,m}$ that are ordered by the forcing-to-response amplification given by the corresponding singular value $\sigma_{n,\omega,m}$. Here, the subscript m denotes the order of resolvent mode. To relate this gain analysis to the velocity fields, each Fourier projection of the nonlinear terms is decomposed as a sum of singular forcing modes

$$\mathbf{f}_{n,\omega} = \sum_m \chi_{n,\omega,m} \boldsymbol{\phi}_{n,\omega,m}, \tag{6}$$

where the unknown forcing coefficients $\chi_{n,\omega,n}$ represent the nonlinear interactions sustaining the turbulence. The fluctuating velocity field is then reconstructed as a weighted sum of singular response modes

$$\mathbf{u}(x, r, \theta, t) = \int_\omega \sum_n \sum_m \chi_{n,\omega,m} \sigma_{n,\omega,m} \boldsymbol{\psi}_{n,\omega,m}(x, r) e^{i(n\theta - \omega t)} \mathrm{d}\omega \, . \tag{7}$$

We note that the response modes $\boldsymbol{\psi}_{n,\omega,m}$ and forcing modes $\boldsymbol{\phi}_{n,\omega,m}$ are functions of both radial and axial coordinates, unlike the one-dimensional resolvent method.[2–4] For simplicity in the interpretation of the resolvent results shown throughout this letter, the low-rank nature of the resolvent,[2–5] $\sigma_{n,\omega,1} \gg \sigma_{n,\omega,2}$ can be employed in order to approximate the velocity field as

$$\mathbf{u}(x, r, \theta, t) \simeq \int_\omega \sum_n \chi_{n,\omega,1} \sigma_{n,\omega,1} \mathbf{u}_{n,\omega,1}(x, r) e^{i(n\theta - \omega t)} \mathrm{d}\omega \, . \tag{8}$$

Notice that in contrast to other dynamic reduced-order models based on Galerkin projection of the NSE, as in Noack *et al.*,[10] the present analysis is based on the assumption of the mean flow in a statistically steady state. In this context, note that the mean equation reads

$$\mathbf{u_0} \cdot \nabla \mathbf{u_0} - \mathbf{f_0} - \nabla p_0 - Re^{-1} \nabla^2 \mathbf{u_0} = 0 \, , \tag{9}$$

thus the mean flow is a steady solution of this mean equation in the presence of $\mathbf{f_0}$ and no assumptions concerning stability or linearization of the flow are required. Further technical details of this analysis can be found in McKeon *et al.*[3]

The resolvent operator $\mathcal{H}_{n,\omega}$ is discretized following an approach similar to the one described by Trefethen[11] for cylindrical coordinates; a Chebychev spectral collocation method is employed along the pipe diameter, while uniform grid and Fourier differentiation matrices are used in the periodic axial direction. Although the computational cost associated with this discretization rises from $\mathcal{O}(N_r^2)$ to $\mathcal{O}(N_r^2 N_x^2)$, with N_r and N_x being the resolution in the radial and axial direction, respectively, SVD computations of the resolvent operator can still be performed in reasonable times on standard laptops at the present Reynolds number.

The DNS dataset employed for the present work and the mean flow $\mathbf{u_0}$ have been computed from DNS data of pipe flow with length $L = 2\pi D$ at $Re = 10\,000$ ($R^+ = 314$ based on friction velocity) obtained using a spectral element–Fourier numerical discretization in cylindrical coordinates[12] with a second-order velocity-correction scheme for time integration.[13] Although the present resolvent formulation is two-dimensional, the present pipe mean flow remains one-dimensional, hence $\mathbf{u_0} = \mathbf{u_0}(r)$.

McKeon *et al.*[3] suggested that the energetically important wavenumbers in these flows are conservatively estimated using a range of scales $0.1 < k < 2\pi R^+/100$, $2\pi/0.1 < n < 2\pi R^+/10$, and $10/u_0^+(r = 0) < c < 1$, c being the wavespeed normalized with the pipe centerline velocity and k the axial wavenumber. Applying this to the current pipe flow at $R^+ = 314$ leads to a conservative estimation of $0.1 < k < 10$, $1 < n < 100$, and $0.02 < \omega/2\pi < 2.02$. The minimum axial wavenumber is restricted by the pipe length and in this study is $k = 2\pi/L = 1$. Notice that all allowable axial wavenumbers in the model are integer multiples of this fundamental axial wavenumber.

Figures 1(a) and 1(b) show the distribution of the principal amplifications $\sigma_{n,\omega,1}$ in the subset of azimuthal wavenumbers n selected here using the one-dimensional and two-dimensional resolvent models, respectively. Figure 1(a) is produced by searching the maximum amplification at a given (ω, n) across a continuum set of axial wavenumbers k via a one-dimensional resolvent model, whereas Figure 1(b) is constructed with the two-dimensional resolvent model by imposing a finite length $L = 2\pi D$. We note that Figure 1(b) can also be constructed with the one-dimensional model by only using integer multiples of the fundamental axial wavenumber corresponding to the pipe length. While Figure 1(a) shows only a smooth decay in amplification as the azimuthal wavenumbers and frequencies increase, Figure 1(b) presents a sparsity in the amplification with frequency, which is more clearly seen at small azimuthal wavenumbers. For brevity of exposition, all the remaining analysis and results will focus on the azimuthal wavenumber $n = 2$.

Figure 2 shows a cross-section of the distribution of amplification from Figure 1(a) and 1(b) obtained at $n = 2$, featuring a peaky behavior of the two-dimensional resolvent model (see solid
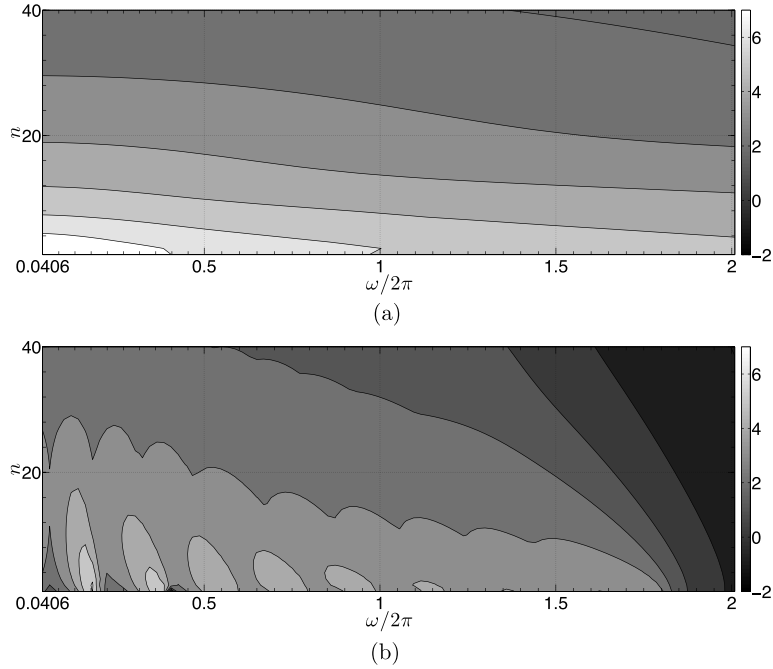
FIG. 1. Distribution of resolvent amplification $\log_{10}(\sigma_{n,w,1})$ in the energetically active subset of azimuthal wavenumbers n and frequencies $\omega/2\pi$ for the first singular vector $m = 1$ at $R^+ = 314$. (a) One-dimensional resolvent model. (b) Two-dimensional resolvent model.

line in Figure 2). The existence of the local amplification peaks can be explained in the two-dimensional resolvent discretization context; while the two-dimensional model effectively restricts the search to wavespeeds $c = \omega/k\mathbf{u_0}(r = 0)$ corresponding to integer multiples of the fundamental axial wavenumber $k = 2\pi/L = 1$, the one-dimensional resolvent model searches the maximum amplification across a continuous range of axial wavenumbers k and thus of mode wavespeeds. Consequently, Figure 2 shows that the one-dimensional model provides a monotonically decaying amplification (see dotted-dashed line in Figure 2).
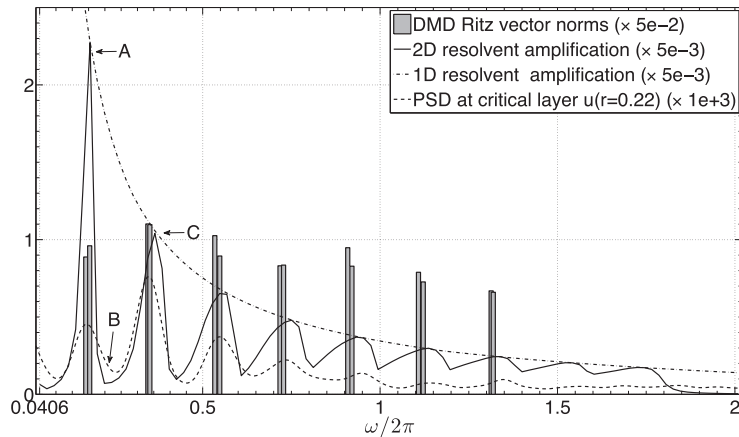

FIG. 2. Distribution of amplification $\sigma_{n,\omega,1}$ in $\omega/2\pi$ at azimuthal wavenumber $n = 2$ for the principal singular mode $m = 1$ at $R^+ = 314$. A, B, and C marks are explained in Figure 3.
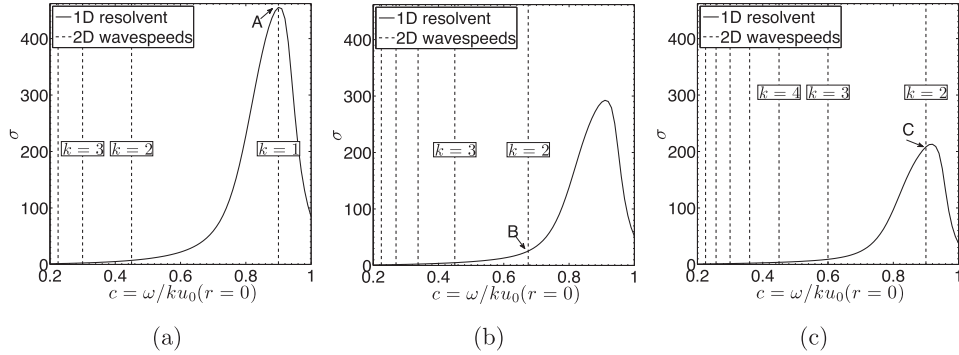
FIG. 3. One-dimensional resolvent amplification versus wavespeed c. Wavespeed c is changed by varying k and keeping frequency $\omega/2\pi$ fixed. Shown for azimuthal wavenumber $n = 2$ at $R^+ = 314$. Vertical dashed lines indicate the discrete wavespeeds corresponding to integer multiple of the fundamental axial wavenumber $k = 2\pi/L$. A, B, and C marks denote the amplification values corresponding to the two-dimensional resolvent in Figure 2. (a) $\omega/2\pi = 0.1826$. (b) $\omega/2\pi = 0.2739$. (c) $\omega/2\pi = 0.3652$.

In order to further explain the origin of the local amplification peaks, Figure 3 shows one-dimensional resolvent amplification versus the wavespeed at different frequencies $\omega/2\pi$ and azimuthal wavenumber $n = 2$, and, at the same time, the possible wavespeeds at that same frequency if a two-dimensional resolvent model is employed. Figures 3(a) and 3(c) demonstrate that a peak in amplification in the two-dimensional resolvent occurs when one of the possible wavespeeds matches a maximum of amplification in the one-dimensional model (marks A and C). Similarly, as seen in Figure 3(b), a local minimum occurs when a maximum distance of the available wavespeeds from the frequency corresponding to the peak is achieved (mark B).

Notice the distinction between the dimensionality of the resolvent and the axial wavenumber discretization effects. In the one-dimensional resolvent, the modes at a given (k, n, ω) are ranked by singular value alone and can assume either a continuous or a discrete set of axial wavenumbers. In contrast, the most amplified modes emerging from the SVD of the two-dimensional resolvent for a given (n, ω) are ranked across different axial wavenumbers k and singular value indices m simultaneously with the additional limitation that the axial wavenumbers can only belong to a discrete set, consisting of integer multiples of the fundamental axial wavenumber restricted by the pipe length. As a result, a discrete selection of axial wavenumbers combined with the one-dimensional resolvent would generate the same sparse amplification in frequency as the two-dimensional resolvent, cf. Figure 3.

As explained by McKeon and Sharma,[2] the maximum amplification in the one-dimensional model takes place at the critical wall-normal location where the wavespeed coincides with the local mean velocity. Figure 3 indicates that the critical layer occurs at a wavespeed $c \simeq 0.9$, which corresponds to a radial location $r \simeq 0.22$. This result, combined with the restriction of possible axial wavenumbers, enables the prediction of the peak locations in a two-dimensional context. For example, Table I lists the frequencies corresponding to the observed amplification peaks in Figure 2 and their theoretical prediction based on the critical layer framework,[2] where a clear correspondence is found between the two lists of frequencies.

In the absence of a link between amplified frequencies and energetically dominant frequencies without assumption on the nonlinear contributions $\chi_{n, \omega, 1}$, a temporal Fourier analysis of the DNS data has been carried out in order to provide insight into this relationship. Given that the largest response occurs at the critical layer, the streamwise velocity at $r = 0.22$ has been selected for the analysis. Figure 2 shows also the power spectral density (PSD) of the streamwise velocity of the Fourier mode $n = 2$ at the critical layer. The good agreement between the most amplified frequencies and the most energetic frequencies provides further evidence to the link between amplified modes and energetically dominant modes.

TABLE I. Comparison between observed frequencies corresponding to amplification peaks and their theoretical prediction using the critical layer framework. Listed for azimuthal wavenumber $n = 2$ at $R^+ = 314$. Critical layer is located at $r = 0.22$ with wavespeed $c(r = 0.22) = 0.9$.

Streamwise wavenumber k	1	2	3	4	5	6
Observed $\omega/2\pi$ from Figure 2	0.1826	0.3653	0.5479	0.7508	0.9334	1.1364
Predicted $\omega/2\pi = 0.9k\mathbf{u_0}(r=0)/2\pi$	0.1826	0.3652	0.5478	0.7304	0.9130	1.0956

A DMD analysis has been applied to the Fourier mode $n = 2$ of the same direct numerical simulation dataset in order to obtain flow structures. The DMD algorithm based on the SVD of the snapshot matrix[8] has been used and the employed dataset consists of 1200 DNS snapshots equispaced during $\mathcal{O}(45)$ wash-out times. Figure 2 also shows the norm of the most energetically relevant DMD Ritz vectors and their associated frequencies, which also agrees with the frequencies predicted by the resolvent model and those found by PSD analysis. Notice that although each bar in Figure 2 is associated with a complex DMD eigenvalue, they appears in pairs because each one corresponds to a different sense of azimuthal rotation ($\pm n$). Another interesting observation is that the norms of these energetically relevant modes do not significant differ. This indicates that the nonlinear forcing coefficients $\chi_{n,\omega,1}$ have a significant influence on the energy distribution. This effect is also observed in the PSD results, as the magnitudes of the peaks are not directly proportional to the corresponding amplification, i.e., the energy corresponding to the second local peak is higher than in the first one.

Figure 4 represents isosurfaces of the DMD eigenmodes associated with the first three amplification peaks and their comparison with their corresponding resolvent modes predicted by the two-dimensional resolvent model. A very good agreement between these structures can be observed.
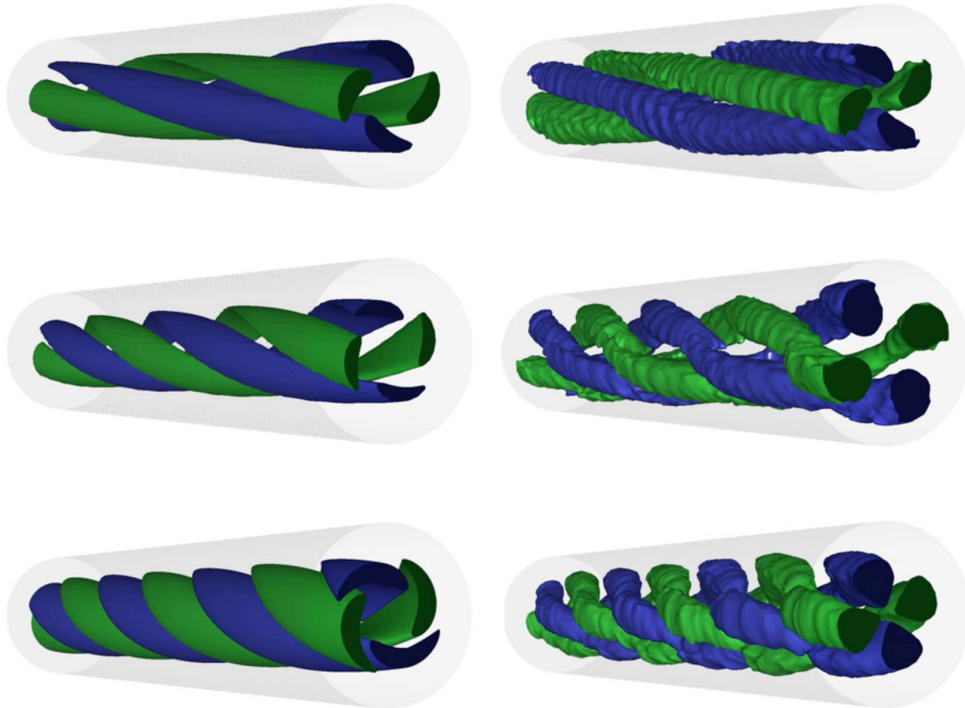

FIG. 4. Comparisons between resolvent modes (*left*) and DMD modes (*right*) at same frequencies $\omega/2\pi = 0.1826$ (*top*) $\omega/2\pi = 0.3652$ (*middle*) $\omega/2\pi = 0.5479$ (*bottom*) at $n = 2$. Colored isosurfaces indicate $\pm 1/3$ of maximum streamwise fluctuating velocity.

Consistently with the critical layer mechanism, each dominant mode presents an axial wavenumber proportional to its associated frequency, maintaining the critical wavespeed $c \simeq 0.9$, as Figures 3(a) and 3(c) indicate, and their largest amplitude is located around the critical layer. Notice that, despite the fact that no axial wavenumber restriction has been imposed on the resolvent modes, the resolvent modes only present a single axial wavenumber, as Figure 4 also shows. In contrast, the DMD modes feature the same dominant axial wavenumber with a contribution of higher wavenumbers, corresponding to other resolvent modes.

In conclusion, it has been shown that the sparsity in frequency observed by Bourguignon *et al.*[1] is a consequence of a finite length periodic domain in the DNS and this property can be exploited; a link between the most amplified sparse frequencies predicted by the resolvent model and the most energetically relevant frequencies in DNS have been provided. Therefore, the energy sparsity in frequency domain and their associated flow structures can be employed in the design of reduced-order models of turbulent flows based on the selection of the most amplified modes emerging from the resolvent decomposition, with the potential to drastically decrease the computational costs required to represent turbulent flows. Mathematically, this leads to reducing the resolvent decomposition in (8) as

$$\mathbf{u}(x, r, \theta, t) \simeq \sum_{(\omega, n) \in \mathcal{S}} \chi_{n,\omega,1} \sigma_{n,\omega,1} \mathbf{u}_{n,\omega,1}(x, r) e^{i(n\theta - \omega t)} \Delta\omega \,, \tag{10}$$

where $\mathcal{S}$ denotes the energetically relevant subset of (ω, n) wavenumbers, which can be identified by means of the present two-dimensional discretization. The small size of $\mathcal{S}$ and thus, the potential to reduce computational expense, can be inferred from a comparison between Figures 1(a) and 1(b). It has been observed that the forcing coefficients $\chi_{n, \omega, m}$ play a major role in the energy distribution in frequency. The study of these unknown nonlinear contributions $\chi_{n, \omega, m}$, which are the last step necessary for the completion of the reduced-order model (10), is currently under way by means of projections of the response modes onto the DNS dataset.

Finally, we recall that the mean velocity profile is required as input data for the resolvent. As a consequence, a successful representation of the fluctuating velocity based on (10) will self-sustain and thus recover the mean velocity characteristics that were assumed in the resolvent.

[1] J.-L. Bourguignon, J. Tropp, A. S. Sharma, and B. J. McKeon, "Compact representation of wall-bounded turbulence using compressive sampling," Phys. Fluids **26**, 015109 (2014).

[2] B. J. McKeon and A. S. Sharma, "A critical layer framework for turbulent pipe flow," J. Fluid Mech. **658**, 336–382 (2010).

[3] B. J. McKeon, A. S. Sharma, and I. Jacobi, "Experimental manipulation of wall turbulence: A systems approach," Phys. Fluids **25**, 031301 (2013).

[4] A. S. Sharma and B. J. McKeon, "On coherent structure in wall turbulence," J. Fluid Mech. **728**, 196–238 (2013).

[5] R. Moarref, A. S. Sharma, J. Tropp, and B. J. McKeon, "Model-based scaling of the streamwise energy density in high-Reynolds-number turbulent channels," J. Fluid Mech. **734**, 275–316 (2013).

[6] M. Luhar, A. S. Sharma, and B. J. McKeon, "Opposition control within the resolvent analysis framework," J. Fluid Mech. **749**, 597–626 (2014).

[7] G. Berkooz, P. Holmes, and J. L. Lumley, "The proper orthogonal decomposition in the analysis of turbulent flows," Annu. Rev. Fluid Mech. **25**, 539–575 (1993).

[8] P. J. Schmid, "Dynamic mode decomposition of numerical and experimental data," J. Fluid Mech. **656**, 5–28 (2010).

[9] C. W. Rowley, I. Mezić, S. Bagheri, P. Schlatter, and D. S. Henningson, "Spectral analysis of nonlinear flows," J. Fluid Mech. **641**, 115–127 (2009).

[10] B. Noack, K. Afanasiev, M. Morzyński, G. Tadmor, and F. Thiele, "A hierarchy of low-dimensional models for the transient and post-transient cylinder wake," J. Fluid Mech. **497**, 335–363 (2003).

[11] L. N. Trefethen, *Spectral Methods in MATLAB* (SIAM, 2000).

[12] H. M. Blackburn and S. Sherwin, "Formulation of a Galerkin spectral element–Fourier method for three-dimensional incompressible flows in cylindrical geometries," J. Comput. Phys. **197**, 759–778 (2004).

[13] G. E. Karniadakis, M. Israeli, and S. A. Orszag, "High-order splitting methods for the incompressible Navier–Stokes equations," J. Comput. Phys. **97**, 414–443 (1991).